A lipid transfer protein knockout library reveals ORP9-ORP11 dimer mediating PS/PI(4)P exchange at the ER-*trans* Golgi contact site to promote sphingomyelin synthesis

Authors:

Birol Cabukusta[1,§], Shalom Borst Pauwels[1], Jimmy J.L.L. Akkermans[1], Niek Blomberg[3], Aat A. Mulder[2], Roman I. Koning[2], Martin Giera[3] and Jacques Neefjes[1]

[1]Cell and Chemical Biology, Oncode Institute, Leiden University Medical Center, Leiden, Netherlands
[2] Electron Microscopy Facility, Cell and Chemical Biology, Leiden University Medical Center, Leiden, Netherlands
[3]Centre for Proteomics and Metabolomics, Leiden University Medical Center, Leiden, Netherlands
[§]Correspondence to b.cabukusta@lumc.nl

Abstract
Numerous lipids are heterogeneously distributed among organelles. Most lipid trafficking between organelles is achieved by a group of lipid transfer proteins (LTPs) that carry lipids using their hydrophobic cavities. LTPs localize at membrane contact sites (MCS) where donor and acceptor organelles form a synapse to exchange information and material. The human genome encodes 90 intracellular LTPs responsible for lipid trafficking and the function of many LTPs in defining cellular lipid levels and distributions is unclear. We created a gene knockout library targeting intracellular LTPs and performed whole-cell lipidomics analysis. This analysis identified major sphingolipid imbalances in ORP9 and ORP11 knockout cells, two proteins of unknown function in sphingolipid metabolism. ORP9 and ORP11 form a heterodimer to localize at ER-*trans* Golgi membrane contact sites. Here, ORP9-ORP11 dimer exchanges phosphatidylserine (PS) for phosphatidylinositol-4-phosphate (PI(4)P) between the two organelles, as a critical step in sphingomyelin synthesis in *trans* Golgi membranes. Overall, our LTP knockout library toolbox identifies various proteins controlling cellular lipid levels including the ORP9-ORP11 heterodimer linking phospholipid and sphingolipid metabolisms at ER-Golgi MCS interphase.

Main Text

The human genome encodes over 140 LTPs, and new LTPs and families are being characterized every so often[1–5]. About 50 of these proteins are secreted and are involved in carrying small molecules in blood plasma[6]. The remaining 90 intracellular LTPs are mainly responsible for intracellular lipid trafficking among organelles. To address the knowledge gap regarding LTPs, we created an arrayed CRISPR/Cas9 knockout library targeting LTPs. In this library, we targeted only the intracellular LTPs and excluded LIPOCALIN and LBP-BPI-CETP families of extracellular proteins. In the library, 90 wells of a 96-well plate were used for targeting intracellular LTPs and 6 for non-targeting (NT) controls (Fig. 1A). We applied the LTP knockout library to MelJuSo, a human subcutaneous melanoma cell line. The efficiency of the knockout strategy was confirmed by the Western blotting of selected wells (Fig. 1B).

To study the function of individual LTPs in defining cellular lipid compositions, we performed whole-cell lipidomics analysis of the LTP knockout cells. To this end, library-generated MelJuSo cells were grown in lipid-depleted serum and analysed using a lipidomics platform thrice on average monitoring 17 different lipid classes. We validated that hexosylceramide detected by lipidomics correspond to glucosylceramide in MelJuSo cells (Fig. S1). Next, we calculated z-scores within each lipid class based on their detected abundance. This analysis revealed many LTP knockout cells with lipid imbalances (Fig. 1C, Fig. S2A-B). Meanwhile, no z-score above the absolute value of 2 was observed for NT control cells (Fig. S2C). Overall, the lipidomics analysis of the LTP knockout library uncovered numerous candidate regulators of cellular lipid levels.

Amongst these candidate regulators of cellular lipid levels, those related to sphingolipid metabolism are notable. This is likely due to many enzymatic steps of sphingolipid metabolism being more linear and lacking the elasticity of phospholipids[7,8]. We found GLTP knockouts with lowered glucosylceramide levels[9] (Fig. 1D, Fig. S3A-C). In addition, we observed NPC1 and NPC2 knockout cells with elevated sphingolipid levels (Fig. 1E). Mutations in *NPC1* and *NPC2* genes cause the lysosomal storage disease Niemann-Pick disease, type C that leads to lysosomal cholesterol accumulation[10]. Cells lacking NPC1 or NPC2 function also accumulate sphingolipids[11]. The elevated total sphingolipid levels were observed globally in all sphingolipid classes without significantly affecting phospholipid levels (Fig. 1F, Fig. S3D).

To confirm whether this phenotype is associated with lysosomal accumulation of sphingolipids, we used a sphingomyelin-binding biosensor (Fig. S3E)[12,13]. Immunofluorescence staining of NPC1 and NPC2 knockout cells using this biosensor revealed lysosomal accumulation of sphingomyelin (Fig. 1G). Flow cytometry analysis using the sphingomyelin biosensor and the GM1 glycosphingolipid biosensor demonstrated that sphingolipid accumulation is also reflected on the cell surface (Fig. 1H, I). Whereas the surface protein levels were not altered as detected by staining for the tetraspanin CD63. Collectively, our results corroborate sphingolipid accumulation in NPC1 and NPC2 deficient cells and illustrate that the LTP knockout library is a viable tool to study LTPs and their role in regulating cellular lipid levels.

Sphingomyelin, the major sphingolipid in mammalian cells, is synthesized in the *trans* Golgi from ceramide delivered from the ER. This non-vesicular trafficking of ceramide is mediated by the ceramide transfer protein CERT[14,15] (Fig. 2B). Our analysis identified CERT knockouts with the lowest sphingomyelin levels (Fig. 1C, 2A). These cells also demonstrate increased glucosylceramide levels, likely as a compensation mechanism (Fig. 2A). In addition, we found ORP9 and ORP11 knockout cells with decreased sphingomyelin and increased glucosylceramide levels – two proteins with an unknown role in sphingolipid metabolism (Fig. 1C, 2A). The sphingolipid imbalances in all three knockout cells were also represented in many sphingolipid species (Fig. 2C, Fig. S4B). Lowered sphingomyelin levels of the knockout cells were further confirmed by their sensitivity towards methyl-β-cyclodextrin treatment (Fig. 2D). Meanwhile, none of the knockout cells demonstrated phospholipid imbalances to a compelling degree (Fig. S4A).

The observation that ORP9 and ORP11 knockout cells mimic CERT knockouts implied a role for ORP9 and ORP11 in *de novo* sphingomyelin synthesis, whereas loss of either ORP9 or ORP11 did not reduce CERT protein levels (Fig. 2E). ORP9 and ORP11 each contain a PH domain mediating localization at the *trans* Golgi, the site of *de novo* sphingomyelin synthesis (Fig.2F, G). As loss of either ORP9 or ORP11 did not alter the

Golgi ultrastructure as detected by light or electron microscopy (Fig. S5), it further suggested that ORP9 and ORP11 regulate sphingomyelin levels by a previously unknown mechanism.

ORP9 and ORP11 interact with each other via their regions between their PH and ORD domains[16]. AlphaFold and the PCOILS coiled coils prediction tool suggested that ORP9 and ORP11 contain two alpha helices each in this region – hereafter referred as "*coils*" (Fig. 3A, S6A, B). AlphaFold-Multimer further suggested that the coils of ORP9 and ORP11 interact with each other (Fig. 3B, S6C-D). Identical analysis of the full-length proteins predicted that the coils drive dimerization of the two proteins (Fig. S6E-G). This was tested by targeting the coils of ORP9 to the mitochondrial outer membrane. In cells expressing mitochondria-targeted ORP9 coils, the coils of ORP11 located to this organelle (Fig. 3C, D). The absence of either coil prevented this colocalization, suggesting that the coils of ORP9 and ORP11 are sufficient for dimerization. This finding was further validated by co-immunoprecipitations (Fig. 3E).

ORP9, but not ORP11, contains a FFAT, two phenylalanines in an acidic tract, motif that drives endoplasmic reticulum (ER) localization by interacting with the ER-resident VAPA and VAPB[17]. Despite not containing a FFAT motif, ORP11 could interact with VAPA and VAPB by its dimerization with ORP9. We tested this by co-immunoprecipitations, where ORP11 could be co-isolated with VAPA from cells expressing VAPA, ORP9 and ORP11 (Fig. 3F). This interaction was diminished significantly when ORP9 was not co-expressed. Furthermore, a VAPA mutant unable to interact with FFAT motifs failed to interact with either ORP9 or ORP11, showing that ORP11 interacts with VAPA indirectly via the ORP9-FFAT motif.

We and others previously showed that in addition to VAPA and VAPB, the human proteome contains three other proteins interacting with FFAT and related short linear motifs: MOSPD1, MOSPD2 and MOSPD3[18,19]. In our earlier efforts to identify interaction partners of VAPA, VAPB and other motif-binding proteins, we performed BioID, proximity biotinylation followed by proteomics, identification of membrane contact sites proteins[19]. In this analysis, ORP9 and ORP11 were found in proximity with VAPA and VAPB but not with other motif-binding proteins (Fig. S7A). This further confirmed that despite lacking a FFAT motif, ORP11 together with ORP9 is part of VAPA- and VAPB-mediated membrane contact sites.

The Golgi localization of ORP9 and ORP11 is mediated by their PH domain interacting with phosphatidylinositol phosphates. We observed the PH domains of ORP9 and ORP11 localizing only partially to the Golgi, unlike the OSBP- and CERT-PH domains that show exclusive localization to this organelle[20,21] (Fig. 3G, S8B). We hypothesized that the dimerization of ORP9 and ORP11 is a mechanism to increase their avidity towards *trans* Golgi membranes. To test this, we created a chimera containing ORP9- and ORP11-PH domains that localized to the Golgi more efficiently than the individual PH domains (Fig. 3G, H). This also implied that loss of either protein should reduce the other's localization to the *trans* Golgi. Immunofluorescence staining of ORP9 and ORP11 knockout cells confirmed that both ORP9 and ORP11 are required for the Golgi localization of the other protein (Fig. 3I-L). Meanwhile, loss of either protein did not influence the levels of the other (Fig. 2E). Our results collectively show that the dimerization of ORP9 and ORP11 via their coils is required for the localization of ORP9-ORP11 dimer to the ER and the *trans* Golgi simultaneously.

ORP9 and ORP11 belong to the OSBP-related protein (ORP) family that transfers sterols or PS while transferring phosphoinositides in the opposite direction[22–25] (Fig. 4A, B). ORP9 and ORP11 carry the conserved PS binding site and are recently shown to relocate to site of lysosomal damage to supply PS for membrane repair[26]. Using an *in vitro* lipid transfer assay, we confirmed that the lipid transfer domains (ORD) of ORP9 and ORP11 are sufficient to traffic PS *in vitro* (Fig. 4C, D, S8A). Moreover, the PS-trafficking activity of ORDs were improved when acceptor liposomes were decorated with PI(4)P (Fig. 4E). This indicates that ORDs of ORP9 and ORP11 transport PI(4)P in the opposite direction of PS trafficking as PI(4)P exchange drives PS transport of ORPs[27,28].

PS is synthesized in the ER and its concentration increases along the secretory pathway as it is enriched on the cytosolic leaflet of the plasma membrane[7]. PI(4)P, on the other hand, is abundant in the *trans* Golgi, where it recruits many proteins to this membrane. While transferring cholesterol from the ER to the *trans* Golgi, OSBP also counter transports PI(4)P to the ER for its hydrolysis by the ER-resident PI(4)P phosphatase SAC1 (Fig. 5K). Homologous to OSBP, ORP9-ORP11 protein complex resides in the ideal intracellular interface to traffic

PS in anterograde and PI(4)P in retrograde direction between the ER and *trans* Golgi (Fig. 5K). This also suggested that the loss of either protein would cause PS and PI(4)P imbalances between the ER and *trans* Golgi. This was tested by using PI(4)P and PS biosensors[29,30] (Fig. S8B). Golgi localization of these sensors indicated PI(4)P accumulation in the Golgi of the ORP9 or ORP11 knockout cells (Fig. 4F, G). Also, PS levels were decreased in the Golgi of these cells (Fig. 4H, I). Furthermore, either phenotype could be rescued by reconstitution of the missing protein (Fig. 4G, I, S8). Overall, this suggests that ORP9-ORP11 dimer is required for maintaining PS and reducing PI(4)P levels in the Golgi apparatus.

Next, we set out to investigate the possible role of ORP9 and ORP11 in regulating cellular sphingomyelin levels. We observed that ORP9 and ORP11 knockout cells did not have reduced sphingomyelin synthesis capacity detected in their lysates, similar to CERT knockouts (Fig. 5A, B). Whereas, all knockouts demonstrated increased glucosylceramide synthesis capacity, further substantiating the lipidomics analysis (Fig. 2A). Unaltered sphingomyelin synthesis capacity was further supported by the protein and mRNA levels for both human sphingomyelin synthases SMS1 and SMS2 (Fig. S9A, B).

SMS1 is localized at the *trans* Golgi, while SMS2 shows dual localization at the plasma membrane but also at the *trans* Golgi[31]. As the enzymatic activity assay in lysates reports on the global sphingomyelin synthesis capacity, we next investigated *de novo* sphingomyelin synthesis that occurs at the *trans* Golgi, where ORP9-ORP11 also localizes. For this purpose, we chased the metabolic fate of palmitic acid alkyne, the precursor of sphinganine and all sphingolipids (Fig. 2B). To enter the sphingolipid pathway, palmitic acid first needs to travel to the ER and later to the Golgi for conversion to sphingomyelin, unlike ceramide analogues, such as NBD-ceramide, that can be converted to sphingomyelin by the plasma membrane-resident SMS2. Furthermore, the palmitic acid alkyne does not contain a bulky fluorescent group and the terminal alkyne allows visualization by click chemistry (Fig. 5C). Using this method, we further confirmed the reduced *de novo* sphingomyelin synthesis in CERT knockout cells (Fig. 5C, D). In addition, ORP9 and ORP11 knockouts also showed decreased conversion of palmitic acid to sphingomyelin, suggesting a similar defect as CERT knockouts.

The observations that loss of ORP9 or ORP11 does not affect CERT protein (Fig. 2E) or reduce CERT localization to the Golgi (Fig. S10) implied that CERT-mediated transfer routes are not affected in ORP9/ORP11 knockouts. Lipidomics analysis showing accumulation of ceramide and glucosylceramide in ORP9/ORP11 knockouts further suggested the conversion of ER-bound ceramides to sphingomyelin in the Golgi is hampered.

To distinguish between two possibilities that may result in lowered sphingomyelin levels –a ceramide delivery defect to the *trans* Golgi and an inability to convert ceramide to sphingomyelin in the *trans* Golgi, we established an immunoisolation protocol for *trans* Golgi membranes. These isolates were enriched for *trans* Golgi marker Golgin-97 and were devoid of other organelle markers, such as the ER, mitochondria and lysosomes (Fig. 5E). We confirmed the membrane integrity of Golgin-97-enriched fractions by their sphingomyelin synthase activity, performed by multi-pass transmembrane proteins (Fig. S11A). Lipidomics analysis of these fractions further confirmed that loss of ORP11 and especially that of ORP9 results in lowered PS levels in the *trans* Golgi, further substantiating our observations (Fig. 4H, I 5F, S11B, C, S12A). The *trans* Golgi fractions also showed reduced sphingomyelin levels, confirming the limited *de novo* sphingomyelin synthesis (Fig. 5C, D, G, S12B). Moreover, the analysis showed elevated ceramide levels in these fractions (Fig. 5H, S12C), demonstrating that the knockouts do not have a ceramide delivery defect but instead a lowered capacity to convert ceramide to sphingomyelin in their *trans* Golgi membranes. This was further confirmed by performing sphingomyelin synthase activity assay in the isolated Golgi membranes, where supplying excess substrate to these membranes bypasses the ceramide delivery routes (Fig. 5I, J). This assay further substantiated that the Golgi of ORP11 and especially of ORP9 knockout cells have a lowered sphingomyelin synthesis capacity. Meanwhile, localization of both sphingomyelin synthases was not reduced in the Golgi, as detected by three different antibodies (Fig. S13). Collectively, our results indicate that PS-PI(4)P exchange between the ER and *trans* Golgi mediated by the ORP9-ORP11 LTP complex is critical for *de novo* sphingomyelin synthesis in *trans* Golgi.

LTPs often localize at MCS to facilitate lipid exchanges between organelles. We found ORP9 and ORP11 localizing at ER-*trans* Golgi contact sites to exchange PS and PI(4)P. We further show that ORP9-ORP11

dimerization is critical for their contact site localization, and consequently, loss of either protein is sufficient to disturb PS/PI(4)P levels in the Golgi, which in return reduces sphingomyelin synthesis capacity. The contact site localization of ORP9-ORP11 dimer is homologous to that of ORP9-ORP10 dimer localizing at ER-endosome contact sites. ORP10 also lacks a FFAT motif and interacts with ORP9[32]. In both LTP complexes, ORP9 provides the FFAT motif required for ER contact. Compared to ORP11 knockout cells, ORP9 knockout cells provide more pronounced phenotypes of cellular sphingolipid imbalances (sphingomyelin and glucosylceramide), phospholipid imbalances in the Golgi apparatus (PS and PI(4)P), as well as reduced capacity of sphingomyelin synthesis in *trans* Golgi membranes. This is most likely due to ORP9 providing a critical factor, i.e. the FFAT motif, for MCS localization, whereas it is possible the loss of ORP11 can be partially compensated by ORP10. ORP10 can also deliver PS to Golgi membrane[33], however our lipidomics analysis of ORP10 knockout cells did not demonstrate any sphingolipid imbalances. In response to lysosomal membrane damage, ORP9, ORP10 and ORP11, together with OSBP and ORP1L localize at the lysosomal membrane to provide PS and other lipids for the repair of the damaged membrane. This localization is driven by the burst of PI(4)P generated as a result of membrane damage, highlighting the role of PI(4)P in spatiotemporal control of lipid trafficking and membrane contact site formation[26,34].

Asymmetric distribution of lipids between two bilayer leaflets is a characteristic feature of the plasma membrane. This is owed to the build-up of sphingomyelin and cholesterol on the outer leaflet and PS on the inner leaflet[7]. The transition of the thin, symmetrical ER membrane to a thicker, rigid and asymmetrical one takes place in the Golgi[7]. Sphingolipid, cholesterol and PS concentrations also increase along the secretory pathway. Various mechanisms are described to drive the sphingolipid and cholesterol trafficking against the concentration gradient, including thermodynamic trapping of cholesterol due to complex formation with sphingomyelin or energy release from the retrograde trafficking of PI(4)P followed by its dephosphorylation in the ER[7,23,35]. The same PI(4)P gradient between the ER and Golgi could also power the anterograde trafficking of PS, which, unlike sphingomyelin or cholesterol, is still exposed on the cytosolic leaflet of the Golgi – thus, maintaining lipid trafficking against the gradient requires energy. Our findings collectively reveal further intertwining of lipid gradients along the secretory pathway at the ER-*trans* Golgi membrane contact sites.

Conflict of Interest:
Authors declare no conflict of interest.

Acknowledgements:
Authors thank Ruud Wijdeven, Robbert Kim, Carolina Jost and the members of the Neefjes lab for their technical and critical input.

Materials and methods

Library design and generation

Targeting and non-targeting guide sequences (Supplementary Table 1) were obtained from the Brunello Human CRISPR Knockout Pooled Library [https://www.addgene.org/pooled-library/broadgpp-human-knockout-brunello/ ; 26780180] and cloned into lentiCRISPR v2 plasmid [https://www.addgene.org/52961/ ; 25075903] as described previously[36]. To increase the efficiency of the gene disruption, we used 3 guide RNAs per gene – a method also used by others to increase the frequency of gene disruption[37]. Cloning of guide RNAs were individually confirmed by Sanger sequencing.

Cell culture

MelJuSo and HEK293T (ATCC CRL-3216) cells were cultured in IMDM (Gibco #21980) and DMEM (Gibco #41966) supplemented with 8% fetal calf serum (Biowest #S1810), respectively. MelJuSo cell line authentication was performed by Eurofins Genomics (19-ZE-000487).

Library Transduction

HEK cells were seeded on a 96-well plate on the day before transfection and transfected with library plasmids and lentiviral packaging plasmids pRSVrev, pHCMV-G VSV-G, and pMDLg/pRRE using polyethyleneimine (Polysciences #23966). Virus was harvested and MelJuSo cells were transduced in the presence of 4µg/ml polybrene (EMD Milipore #TR-1003-G). Transduced cells were subjected to selection using 2µg/ml puromycin.

Lipid extractions and lipidomics analysis

For lipidomics analysis, knockout and gNT cells were expanded to 15-cm dishes and cultured in IMDM supplemented with lipid-depleted serum (Pel-Freez #37217-5) for 3-4 days. Next, cells were scraped in 2% NaCl solution and lipids were extracted following the Bligh-Dyer protocol. In brief, harvested cells were resuspended in 200µL 2% (w/v) NaCl followed by addition of 500µL methanol and 250µL chloroform. Samples were vortexed for 5 min. Following phase separation by adding 250µL chloroform and 250µL 0.45 % (w/v) NaCl, samples were centrifuged for 5min at 15,000xg. Next, bottom fractions were collected and dried under continuous nitrogen stream prior to lipidomics analysis.

Comprehensive, quantitative shotgun lipidomics was carried out as described in detail elsewhere[38,39]. Briefly, dried lipid extracts were spiked with 54 deuterated internal standards and dissolved in methanol:chloroform 1:1 containing 10 mM ammonium acetate. Lipids are then analysed with a flow injection method at a flow rate of 8 µL/min applying differential ion mobility for lipid class separation and subsequent multiple reaction monitoring in positive and negative electrospray ionization mode. Using the Shotgun Lipidmics Assistant (SLA) software individual lipid conentrations are calculated after correction for their respective internal standards.

Data analysis & statistics

Data analyses were performed using R (4.1.0 "*Camp Pontanezen*") and RStudio (2022.12.0+353) with following packages: ggplot2, dplyr, readr, ggrepel, ggcorrplot2, reshape2, ggbeeswarm, ggthemes, ggsignif, purr, tidyr, tibble, limma, and stringr. Z-scores were calculated using the following formula: $z = (x - \mu)/\sigma$. Golgi lipidomics data were double normalized to the mean of POPC normalized levels from MJS and gNT samples. Raw lipidomics data available at Supplementary Table 2.

Mean values and standard deviations are denoted in all graphs. For statistical analysis, student's t-test is used, unless stated otherwise. *p<0.05, **p<0.01, ***p<0.001, ****p<0.0001.

Co-immunoprecipitation, SDS-PAGE and Western blotting

Co-immunoprecipitation, SDS-PAGE and Western blotting were performed as described previously[19].

Immunofluorescence staining

Immunofluorescence staining was performed as described previously[19]. For equinatoxin staining, cells were fixed with 4%PFA:PBS (v/v) and permeabilized with 10µg/ml digitonin in PBS. Staining was performed in PBS.

Flow cytometry analysis

MelJuSo cells were brought to suspension by trypsinization. Stained with indicated probes on ice prior to analysis using a BD LSR-II equipped with 488 and 561nm lasers.

Electron microscopy

Cells cultured in 6-cm dishes were fixed for an hour at room temperature by adding double concentrated fixative to the medium (final concentration: 1.5% glutaraldehyde in 0.1M cacodylate buffer). After three times rinsing with 0.1 M cacodylate buffer, the cells were postfixed with 1% osmium tetroxide and 1.5% uranyl acetate. Cells are dehydrated with a series of ethanol, followed by a series of mixtures of ethanol and EPON (LX112, Leadd) and at the end pure EPON. BEEM capsules filed with EPON were placed on the dishes with the open face down. After EPON polymerization at 40°C the first night and 70°C the second night, the BEEM capsules were snapped off. Ultrathin sections 80 nm were made parallel to the surface of the BEEM capsules containing the cultured cells. The sections were contrasted with uranyl acetate and lead hydroxide and examined with a Tecnai Twin transmission electron microscope (Thermo Fisher, Eindhoven, Netherlands). Overlapping images were automatically collected and stitched together into a composite image as previously described.[40]

Recombinant protein purification

A codon optimized version of cDNA encoding the non-toxic version of equinatoxin[13] was ordered from IDT technologies. GFP sequence was obtained from meGFP-C1 vector. cDNAs encoding ORD domains of ORP9 and ORP11, and EQT-GFP fusion protein were cloned into a pNKI1.8/GST-expression vector.

E. coli BL21/Rosetta were grown in 2xYT medium and expression was induced when OD_{600} was at 1. Bacterial pellets were lysed by sonication and cleared by centrifugation. Proteins were purified using Glutathione Sepharose™ 4 Fast Flow (GE Healthcare #17-5132-03) and cleaved using 3C protease protein prior to reverse purification using glutathione beads.

Methyl-β-cyclodextrin and MTT viability assay

Cells were seeded in a 96-well plate and were cultured in OptiMEM (ThermoFisher # 31985047) for 3 days. Cells were treated with 10mM methyl-β-cyclodextrin (Sigma #C4555) and cell viability was tested using MTT viability assay (Cayman # 21795). Absorbance at 560nm was measured using a BMG ClarioStar plate reader.

Liposome preparation and lipid transfer assay

Donor liposomes composed of 2% NBD-PS (Avanti #810194), 2% Rhodamine-PE (Avanti #810150), 10% DOPE (Avanti #850725), 86% DOPC (Avanti #850375) and acceptor liposomes composed of DOPC with or without 5% Brain PI(4)P (Avanti #840045) were prepared as follows: Lipids were mixed in a glass container and dried under a constant nitrogen flow to create a film. Lipids were further freeze-dried at least for two hours under vacuum. Next, lipid films were rehydrated in HKM (50mM HEPES pH 7.2; 120mM K-acetate; 1mM $MgCl_2$) buffer for 30 minutes followed by 5 cycles of freeze thaw. Lipids were extruded using Avanti MiniExtruder using a 100nm filter. Uniformity and the concentration of lipids were confirmed using a Wyatt Nanostar Dynamic Light Scattering. For lipid transfer assays, 80µM of each donor and acceptor vesicles were

used in 100µL volume and protein of interest was added in 5µL. NBD fluorescence was measured using a BMG ClarioStar plate reader.

AlphaFold & AlphaFold-multimer

Structure predictions were performed using AlphaFold, AlphaFold-Multimer and ColabFold prediction tools, as described[41–43].

Golgi isolation and quantification of Golgi lipid levels

Cells were washed twice in 0.25M Sucrose and scraped in IM buffer (0.25M Mannitol, 0.5mM EGTA, 5mM HEPES pH 7.4). Samples were passed through a 26xG needle for lysis. Lysates were cleared from nuclei by centrifugation twice at 600xg for 5min. Post-nuclear supernatant was subjected to protein determination using BCA protein determination kit. Equal amounts of protein were supplemented with 150mM NaCl and incubated with Protein A/G Magnetic Beads (ThermoFisher #88802) preloaded either or not with Golgin-97 antibodies. Next, samples were washed 3 times with IM buffer supplemented with 150mM NaCl before lipid extraction or enzymatic activity assay.

siRNA transfections and metabolic chasing of BODIPY-C5-ceramide in intact cells

siRNA transfections were carried out as described previously[19]. siRNA for UGCG (M-006441-02-0005) and UGT8 (M-010270-02-0005) were obtained from Horizon Discovery. MelJuSo cells treated with siRNAs or 10µM PDMP (Cayman #62595)) were washed twice with PBS and incubated with serum-free medium supplemented with 0.25µM BODIPY-C5-Ceramide complexed to BSA (Thermo Fisher #B22650). After 3 hours, cells were subjected to lipid extraction and thin layer chromatography as described below. The following lipids were used as standards: TopFlour-C11-galactosylceramide (Avanti Polar Lipids #810266), TopFlour-C11-glucosylceramide (Avanti Polar Lipid #810267) and BODIPY- C5-Lactosylceramide (Thermo Fisher #B34402).

Metabolic chasing of de novo sphingomyelin synthesis

Cells were incubated with 20µM ethanolic palmitic acid alkyne (Cayman Chemical # 13266) in serum-free medium for 6 hours. Next, cells were washed twice in PBS and scraped in 2%NaCl solution. Lysates were subjected to protein determination using Pierce BCA Protein Kit (Thermo #23225) and equal amounts of proteins were used for lipid extractions as above. For alkaline hydrolysis, dried lipids were resuspended in 200µL methanolic sodium methoxide and incubated at room temperature for 1h. Samples were added 30µL acetic acid/water (1:4, v/v), 120µL 2% NaCl, and 400µL chloroform to re-extract lipids. Dried lipids were resuspended in 15µL chloroform and 65µL of click mix containing 400µM 3-Azido-7-hydroxycoumarin (Baseclick #BCFA-047-1) and 900µM tetrakis(acetonitrile)copper(i) tetrafluoroborate (Sigma #677892) in acetonitrile/ethanol (7:3, v/v) was added and incubated 3h at 45ºC prior to TLC analysis.

Quantitative RT-PCR

RT-PCR was performed as described previously[19] using the following primer sets:
CERT_1: ATGTCGGATAATCAGAGCTGGA / ATCCTGCCACCCATGAATGTA,
CERT_2: TCCATCTGTCTTAGCAAGGCT / GCTGTTCAATGGCATCTATCCA,
SMS1_1: TGTGCCGAGTCTCCTCTGA / CCGTTCTTGTGTGCTTCCAAA,
SMS1_2: CAGCATCAAGATTAAACCCAACG / TGGTGAGAACGAAACAGGAAAG,
SMS2_1: TCCTACGAACACTTATGCAAGAC / CCGGGTACTTTTTGGTGCCT,
SMS2_2: CAAATTGCTATGCCCACTGAATC / GTTGTCAAGACGAGGTTGAAAAC

Enzymatic activity assay in lysates and isolated Golgi fractions

For enzymatic activity measurements in lysates, cells were washed twice in 0.25M Sucrose and scraped in IM buffer (0.25M Mannitol, 0.5mM EGTA, 5mM HEPES pH 7.4). Samples were passed through a 26xG needle for lysis. Lysates were cleared from nuclei by centrifugation twice at 600xg for 5min. Post-nuclear supernatant was subjected to protein determination using BCA protein determination kit. Equal amounts of protein in a 50µL volume were mixed with 50µL IM buffer supplemented with 5µM NBD-C6-ceramide (Avanti Polar Lipids

#8102109) from an ethanolic solution. Reactions were incubated 1h at 37ºC in dark with constant shaking. Next, samples were subjected to lipid extractions and thin-layer chromatography as described. For the enzymatic activity assays in Golgi, isolated Golgi fractions were resuspended in 50µL IM buffer and incubated with NBD-C6-ceramide as above.

Thin-layer chromatography

Dried lipids were spotted on a thin-layer chromatography (TLC) Silica gel 60 (Merck #1.05554.0001) plate and developed in chloroform:methanol:acetone:acetic acid:water (50:10:20:10:5, v/v/v/v/v). Fluorescent images were acquired using a Typhoon FLA9500 equipped with a 488nm laser and a BPB1 filter (530DF20).

Plasmids

Plasmid	***Reference***	***cDNA***	***Backbone***
GST-EQT-GFP	This study		pNKI1.8
Scarlet-ORP9 iso.2	This study	Mouse Osbpl9 isoform 2 cDNA was ordered from Horizon Discovery. BC023759. IMAGE:5344071	mScarlet-C1
Scarlet-ORP11		Human OSBPL11 cDNA was ordered from Horizon Discovery. IMAGE:3916115. BC065213	mScarlet-C1
GFP-OSBP-PH	addgene #49571, ref.[30]		
RFP-LactC2	addgene#74061, ref.[29]		
GFP-CC11	This study		
Mito-tagRFP	This study	cDNA encoding the first 70 amino acids of TOM70 was ordered from IDT technologies.	tagRFP-N1
Mito-CC9-tagRFP	This study		tagRFP-N1
GFP-PH9	This study		meGFP-C1
GFP-PH11	This study		meGFP-C1
GFP-PH9-PH11	This study		meGFP-C1
FLAG-ORP11	This study		FLAG-C1
GST-ORD9	This study		pNKI1.8
GST-ORD11	This study		pNKI1.8
FLAG-VAPA	Ref.[19]		
meGFP-C1	Ref.[19]		
mScarlet-C1	Ref.[19]		
GFP-VAPA	Ref.[19]		
GFP-VAPA**	Ref.[19]		
Scarlet-CERT	Ref.[19]		

Antibodies

Target	**Supplier**	**Catalog #**	**Host**
OSBP	Proteintech	11096-1-AP	Rabbit
ORP1L	PMID: 12631712		Rabbit
CERT	Bethyl	A300-669A	Rabbit
NPC1	Novus	NB400-148	Rabbit
NPC2	Proteintech	19888-1-AP	Rabbit
GLTP	Proteintech	10850-1-AP	Rabbit
PITPNB	Proteintech	13110-1-AP	Rabbit

ORP9	Proteintech	11879-1-AP	Rabbit
STARD7	Proteintech	15689-1-AP	Rabbit
SEC14L1	Proteintech	25541-1-AP	Rabbit
PITNM1	Proteintech	26983-1-AP	Rabbit
SEC14L2	Origene	TA503723	Mouse
TEX2	Bethyl	A304-705A	Rabbit
FAPP2	Proteintech	15410-1-AP	Rabbit
ORP9	Santa Cruz	sc-398961	Mouse
CD63-V450	BD Horizon	561984	Mouse
CTB-Alexa568	Invitrogen	C34777	
Actin	Sigma-Aldrich	A5441	Mouse
GM130	BD Transduction	610823	Mouse
FLAG-HRP	Sigma-Aldrich	A8592	Mouse
GFP	Ref. [19]		Rabbit
Scarlet	ChromoTek	6G6-100	Mouse
tagRFP	Evrogen	AB232	Rabbit
Golgin-97	Invitrogen	A-21270	Mouse
Golgin-97	Cell Signaling	13192S	Rabbit
Calnexin (C5C9)	Cell Signaling	2679	Rabbit
R-PDI	Cell Signaling	3501	Rabbit
TOM20	Proteintech	11802-1-AP	Rabbit
Actin*HRP	Santa Cruz	sc-47778	Mouse
SMS1	Sigma/Aldrich	HPA045191	Rabbit
SMS2	Santa Cruz	sc-293384	Mouse
CERT	Proteintech	15191-1-AP	Rabbit
SGMS1	Proteintech	19050-1-AP	Rabbit
ORP11	Proteintech	11318-1-AP	Rabbit
Anti-mouse Alexa 488	Thermo Fisher	A21202	Donkey
Anti-mouse Alexa 568	Thermo Fisher	A10037	Donkey
Anti-mouse Alexa 647	Thermo Fisher	A21236	Goat
Anti-rabbit Alexa 488	Thermo Fisher	A21206	Donkey
Anti-rabbit Alexa 568	Thermo Fisher	A10042	Donkey
Anti-rabbit Alexa 647	Thermo Fisher	A31573	Donkey
Anti-Mouse IgG, HRP	Thermo Fisher	G21040	Goat
Anti-Rabbit, IgG, HRP	Thermo Fisher	G21234	Goat

References:

1. Gatta, A. T. *et al.* A new family of StART domain proteins at membrane contact sites has a role in ER-PM sterol transport. *Elife* **4**, 1–46 (2015).
2. Sandhu, J. *et al.* Aster Proteins Facilitate Nonvesicular Plasma Membrane to ER Cholesterol Transport in Mammalian Cells. *Cell* **175**, 514-529.e20 (2018).
3. Valverde, D. P. *et al.* ATG2 transports lipids to promote autophagosome biogenesis. *J. Cell Biol.* **218**, 1787–1798 (2019).
4. Osawa, T. *et al.* Atg2 mediates direct lipid transfer between membranes for autophagosome formation. *Nat. Struct. Mol. Biol.* **26**, 281–288 (2019).
5. Yeo, H. K. *et al.* Phospholipid transfer function of PTPIP51 at mitochondria-associated ER membranes. *EMBO Rep.* **22**, (2021).
6. Wong, L. H., Gatta, A. T. & Levine, T. P. Lipid transfer proteins: the lipid commute via shuttles, bridges and tubes. *Nature Reviews Molecular Cell Biology* vol. 20 85–101 (2019).
7. Holthuis, J. C. M. & Menon, A. K. Lipid landscapes and pipelines in membrane homeostasis. *Nature* **510**, 48–57 (2014).
8. van Meer, G. & de Kroon, A. I. P. M. Lipid map of the mammalian cell. *J. Cell Sci.* **124**, 5–8 (2011).
9. Nurmi, H. *et al.* Glycolipid transfer protein knockout disrupts vesicle trafficking to the plasma membrane. *J. Biol. Chem.* **299**, 104607 (2023).
10. Platt, F. M. Sphingolipid lysosomal storage disorders. *Nature* **510**, 68–75 (2014).
11. Newton, J., Milstien, S. & Spiegel, S. Niemann-Pick type C disease: The atypical sphingolipidosis. *Adv. Biol. Regul.* **70**, 82–88 (2018).
12. Sokoya, T. *et al.* Pathogenic variants of sphingomyelin synthase SMS2 disrupt lipid landscapes in the secretory pathway. *Elife* **11**, (2022).
13. Deng, Y., Rivera-Molina, F. E., Toomre, D. K. & Burd, C. G. Sphingomyelin is sorted at the trans Golgi network into a distinct class of secretory vesicle. *Proc. Natl. Acad. Sci. U. S. A.* **113**, 6677–6682 (2016).
14. Hanada, K. *et al.* Molecular machinery for non-vesicular trafficking of ceramide. *Nature* **426**, 803–809 (2003).
15. Kumagai, K. & Hanada, K. Structure, functions and regulation of CERT, a lipid-transfer protein for the delivery of ceramide at the ER–Golgi membrane contact sites. *FEBS Lett.* **593**, 2366–2377 (2019).
16. Zhou, Y. *et al.* OSBP-related protein 11 (ORP11) dimerizes with ORP9 and localizes at the Golgi-late endosome interface. *Exp. Cell Res.* **316**, 3304–3316 (2010).
17. Neefjes, J. & Cabukusta, B. What the VAP: The Expanded VAP Family of Proteins Interacting With FFAT and FFAT-Related Motifs for Interorganellar Contact. *Contact* **4**, 251525642110122 (2021).
18. Di Mattia, T. *et al.* Identification of MOSPD2, a novel scaffold for endoplasmic reticulum membrane contact sites. *EMBO Rep.* **19**, 1–22 (2018).
19. Cabukusta, B. *et al.* Human VAPome Analysis Reveals MOSPD1 and MOSPD3 as Membrane Contact Site Proteins Interacting with FFAT-Related FFNT Motifs. *Cell Rep.* **33**, 108475 (2020).
20. Levine, T. P. & Munro, S. The pleckstrin homology domain of oxysterol-binding protein recognises a determinant specific to Golgi membranes. *Curr. Biol.* **8**, 729–739 (1998).
21. Levine, T. P. & Munro, S. Targeting of Golgi-Specific Pleckstrin Homology Domains Involves Both PtdIns 4-Kinase-Dependent and -Independent Components. *Curr. Biol.* **12**, 695–704 (2002).
22. Wang, H. *et al.* ORP2 Delivers Cholesterol to the Plasma Membrane in Exchange for Phosphatidylinositol 4, 5-Bisphosphate (PI(4,5)P 2). *Mol. Cell* **73**, 458-473.e7 (2019).
23. Mesmin, B. *et al.* A four-step cycle driven by PI(4)P hydrolysis directs sterol/PI(4)P exchange by the ER-Golgi Tether OSBP. *Cell* **155**, 830–843 (2013).
24. de Saint-Jean, M. *et al.* Osh4p exchanges sterols for phosphatidylinositol 4-phosphate between lipid bilayers. *J. Cell Biol.* **195**, 965–978 (2011).
25. Maeda, K. *et al.* Interactome map uncovers phosphatidylserine transport by oxysterol-binding proteins. *Nature* **501**, 257–261 (2013).
26. Tan, J. X. & Finkel, T. A phosphoinositide signalling pathway mediates rapid lysosomal repair. *Nature* **609**, 815–821 (2022).
27. Chung, J. *et al.* PI4P/phosphatidylserine countertransport at ORP5- and ORP8-mediated ER - Plasma membrane contacts. *Science (80-.).* **349**, 428–432 (2015).
28. Von Filseck, J. M. *et al.* Phosphatidylserine transport by ORP/Osh proteins is driven by phosphatidylinositol 4-phosphate. *Science (80-.).* **349**, 432–436 (2015).
29. Yeung, T. *et al.* Membrane phosphatidylserine regulates surface charge and protein localization. *Science* **319**, 210–213 (2008).
30. Moorhead, A. M., Jung, J. Y., Smirnov, A., Kaufer, S. & Scidmore, M. A. Multiple host proteins that function in phosphatidylinositol-4-phosphate metabolism are recruited to the chlamydial inclusion. *Infect. Immun.* **78**, 1990–2007 (2010).
31. Tafesse, F. G., Ternes, P. & Holthuis, J. C. M. The multigenic sphingomyelin synthase family. *J. Biol. Chem.* **281**, 29421–29425 (2006).
32. Kawasaki, A. *et al.* PI4P/PS countertransport by ORP10 at ER–endosome membrane contact sites regulates endosome fission. *J. Cell Biol.* **221**, (2021).
33. Venditti, R. *et al.* Molecular determinants of ER-Golgi contacts identified through a new FRET-FLIM system. *J. Cell Biol.* **218**, 1055–1065 (2019).
34. Radulovic, M. *et al.* Cholesterol transfer via endoplasmic reticulum contacts mediates lysosome damage repair. *EMBO J.* **41**, (2022).
35. Mesmin, B. *et al.* Sterol transfer, PI 4P consumption, and control of membrane lipid order by endogenous OSBP . *EMBO J.* **36**, 3156–3174 (2017).
36. Wijdeven, R. H. *et al.* CRISPR Activation Screening Identifies VGLL3-TEAD1-RUNX1/3 as a Transcriptional Complex for PD-L1 Expression. *J. Immunol.* (2022) doi:10.4049/JIMMUNOL.2100917.
37. Wong, C. H. *et al.* Genome-scale requirements for dynein-based trafficking revealed by a high-content arrayed CRISPR screen. *bioRxiv* 2023.03.01.530592 (2023) doi:10.1101/2023.03.01.530592.
38. Ghorasaini, M. *et al.* Cross-Laboratory Standardization of Preclinical Lipidomics Using Differential Mobility Spectrometry and Multiple Reaction Monitoring. *Anal. Chem.* **93**, 16369–16378 (2021).
39. Su, B. *et al.* A DMS Shotgun Lipidomics Workflow Application to Facilitate High-Throughput, Comprehensive Lipidomics. *J. Am. Soc. Mass Spectrom.* **32**, 2655–2663 (2021).
40. Faas, F. G. A. *et al.* Virtual nanoscopy: generation of ultra-large high resolution electron microscopy maps. *J. Cell Biol.* **198**, 457–469 (2012).
41. Jumper, J. *et al.* Highly accurate protein structure prediction with AlphaFold. *Nature* **596**, 583–589 (2021).
42. Mirdita, M. *et al.* ColabFold: making protein folding accessible to all. *Nat. Methods* **19**, 679–682 (2022).
43. Evans, R. *et al.* Protein complex prediction with AlphaFold-Multimer. *bioRxiv* 2021.10.04.463034 (2022) doi:10.1101/2021.10.04.463034.

A lipid transfer protein knockout library reveals ORP9-ORP11 dimer mediating PS/PI(4)P exchange at the ER-*trans* Golgi contact site to promote sphingomyelin synthesis

Authors:
Birol Cabukusta[1,§], Shalom Borst Pauwels[1], Jimmy J.L.L. Akkermans[1], Niek Blomberg[3], Aat A.Mulder[2], Roman I. Koning[2], Martin Giera[3] and Jacques Neefjes[1]

[1]Cell and Chemical Biology, Oncode Institute, Leiden University Medical Center, Leiden, Netherlands
[2] Electron Microscopy Facility, Cell and Chemical Biology, Leiden University Medical Center, Leiden, Netherlands
[3]Centre for Proteomics and Metabolomics, Leiden University Medical Center, Leiden, Netherlands
[§]Correspondence to b.cabukusta@lumc.nl

Figures

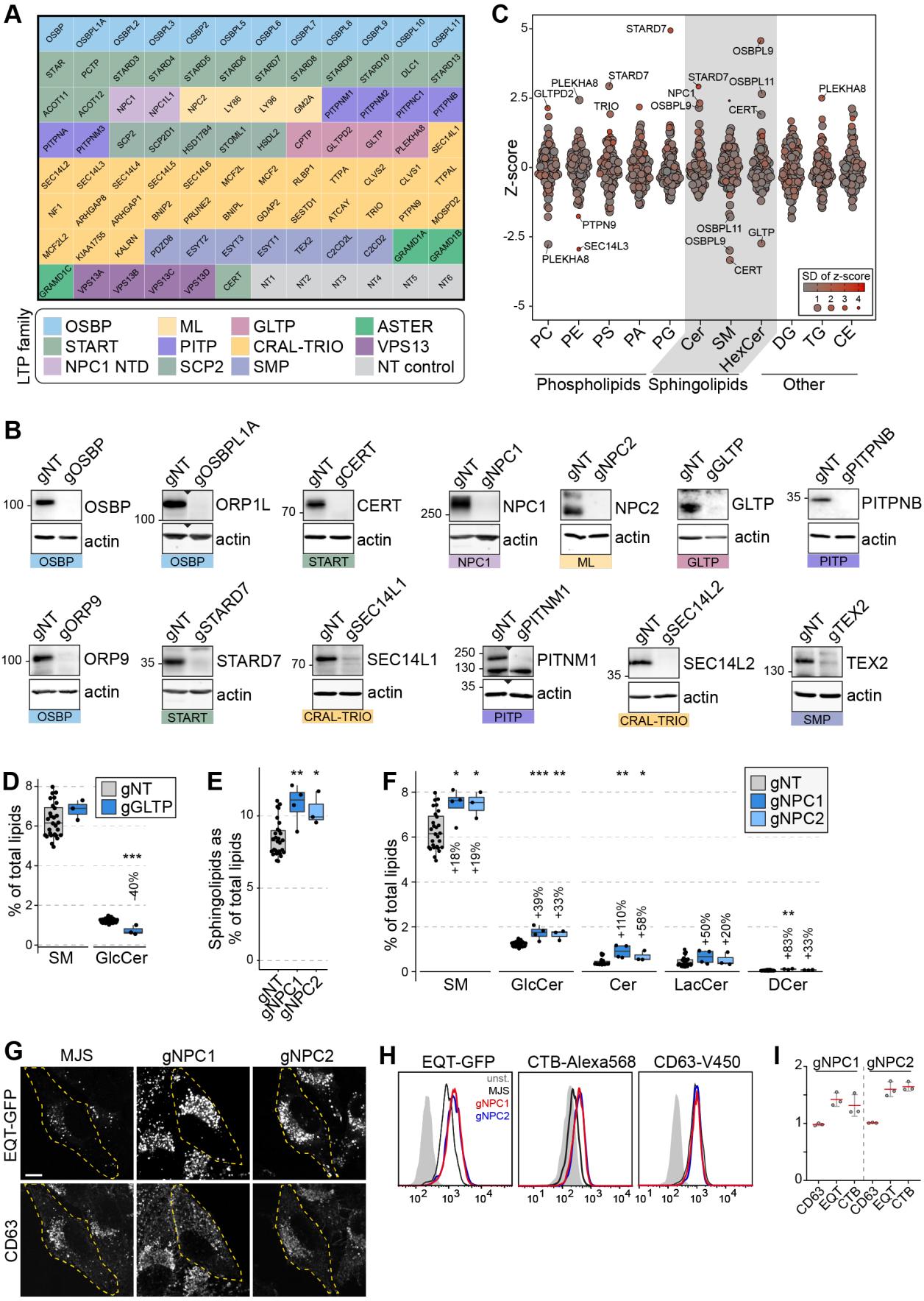
A
OSBP OSBPL1A OSBPL2 OSBPL3 OSBP2 OSBPL5 OSBPL6 OSBPL7 OSBPL8 OSBPL9 OSBPL10 OSBPL11
STAR PCTP STARD3 STARD4 STARD5 STARD6 STARD7 STARD8 STARD9 STARD10 DLC1 STARD13
ACOT11 ACOT12 NPC1 NPC1L1 NPC2 LY86 LY96 GM2A PITPNM1 PITPNM2 PITPNC1 PITPNB
PITPNA PITPNM3 SCP2 SCP2D1 HSD17B4 STOML1 HSDL2 CPTP GLTPD2 GLTP PLEKHA8 SEC14L1
SEC14L2 SEC14L3 SEC14L4 SEC14L5 SEC14L6 MCF2L MCF2 RLBP1 TTPA CLVS2 CLVS1 TTPAL
NF1 ARHGAP8 ARHGAP1 BNIP2 PRUNE2 BNIPL GDAP2 SESTD1 ATCAY TRIO PTPN9 MOSPD2
MCF2L2 KIAA1755 KALRN PDZD8 ESYT2 ESYT3 ESYT1 TEX2 C2CD2L C2CD2 GRAMD1A GRAMD1B
GRAMD1C VPS13A VPS13B VPS13C VPS13D CERT NT1 NT2 NT3 NT4 NT5 NT6
LTP family
OSBP
START
NPC1 NTD
ML
PITP
SCP2
GLTP
CRAL-TRIO
SMP
ASTER
VPS13
NT control
C
Z-score
STARD7
OSBPL9
PLEKHA8
GLTPD2
TRIO
NPC1
OSBPL11
CERT
PTPN9
SEC14L3
GLTP
SD of z-score
PC PE PS PA PG Cer SM HexCer DG TG CE
Phospholipids
Sphingolipids
Other
B
gNT gOSBP
OSBP
actin
gNT gOSBPL1A
ORP1L
gNT gCERT
CERT
gNT gNPC1
NPC1
gNT gNPC2
NPC2
gNT gGLTP
GLTP
gNT gPITPNB
PITPNB
gNT gORP9
ORP9
gNT gSTARD7
STARD7
gNT gSEC14L1
SEC14L1
gNT gPITNM1
PITNM1
gNT gSEC14L2
SEC14L2
gNT gTEX2
TEX2
OSBP
START
CRAL-TRIO
NPC1
ML
GLTP
PITP
SMP
D
% of total lipids
gNT
gGLTP
-40%
SM
GlcCer
E
Sphingolipids as % of total lipids
gNT gNPC1 gNPC2
F
% of total lipids
gNT
gNPC1
gNPC2
+18% +19%
+39% +33%
+110% +58%
+50% +20%
+83% +33%
SM GlcCer Cer LacCer DCer
G
MJS
gNPC1
gNPC2
EQT-GFP
CD63
H
EQT-GFP
CTB-Alexa568
CD63-V450
unst.
MJS
gNPC1
gNPC2
I
gNPC1 gNPC2
CD63 EQT CTB CD63 EQT CTB

Figure 1: Lipidomics analysis of a LTP knockout library revealed known and candidate controllers of cellular lipid levels.
(A) Schematic representation of the arrayed gene knockout library targeting LTPs. (B) Western blotting of the selected wells shows the efficiency of the LTP knockout library on MelJuSo cells. gNT: Non-targeting control cells. (C) Plot of the lipidomics analysis: Z-scores calculated for 11 lipid classes are plotted. Each data point represents an LTP knockout cell line; size and color of data points represent the standard deviation of Z-scores among 3 experiments on average. See Figure S2 for the full panel. PC: phosphatidylcholine, PE: phosphatidylethanolamine, PS: phosphatidylserine, PA: phosphatidic acid, PG: phosphatidylglycerol, Cer: ceramide, SM: sphingomyelin, HexCer: hexosylceramide, DG: diacylglycerol, TG: triacylglycerol, and CE: cholesterol ester. (D) GLTP knockout show decreased glucosylceramide levels. (E) NPC1 and NPC2 knockout cells have increased sphingolipids levels compared to control cells. (F) Increased sphingolipid levels in NPC1 and NPC2 knockouts are represented in all sphingolipid classes. GlcCer: glucosylceramide, LacCer: lactosylceramide, and DCer: dihydroxyceramide. (G) Immunofluorescence images of NPC1 and NPC2 knockout cells permeabilized and stained with recombinant GFP-EQT show the accumulation of sphingomyelin in the lysosomes comparted to the parental MelJuSo (MJS) cells. Pixel intensities of the images were adjusted. Scale bar 10μm. (H) Flow cytometry analysis demonstrating the accumulation of sphingomyelin (EQT-GFP) and glycosphingolipid GM1 (CTB-Alexa568) on the cell surface. (I) Mean fluorescence intensities for each staining normalized to control cells from 3 experiments. Approximately 2000 cells were analyzed per experiment.

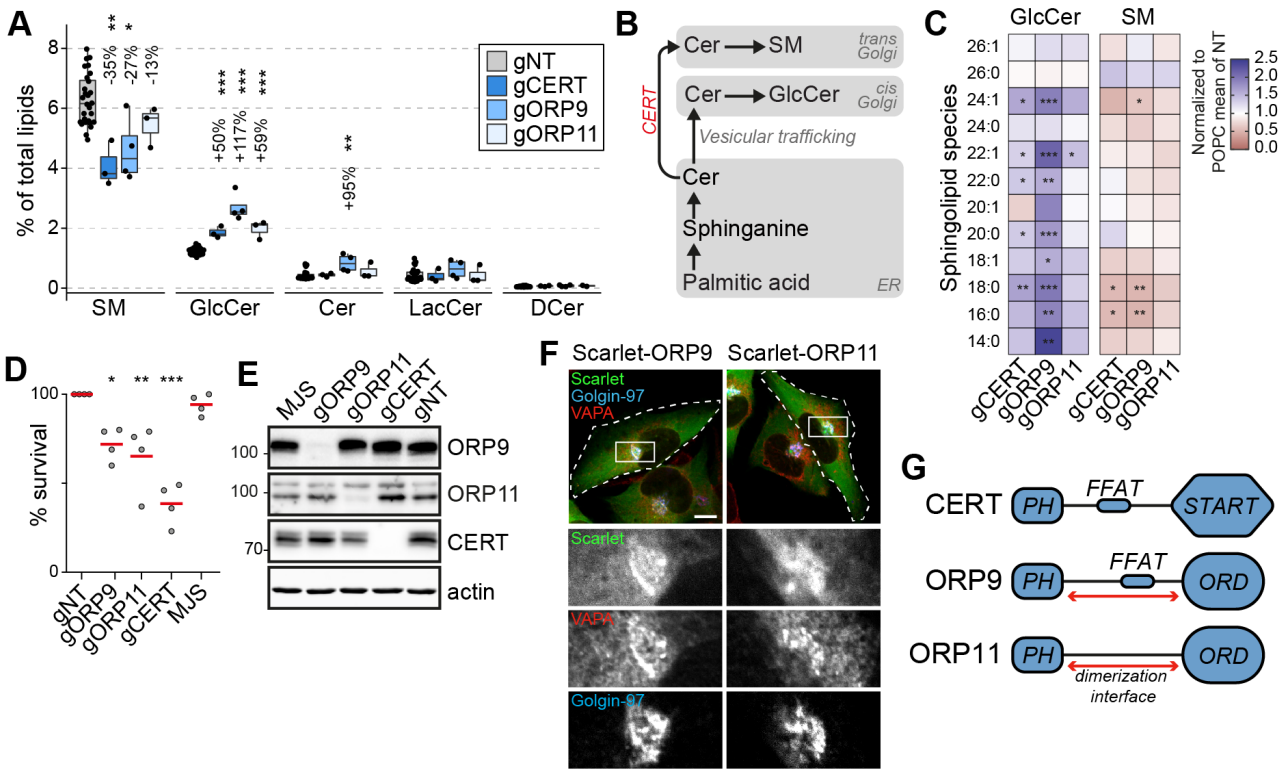

Figure 2: CERT, ORP9 and ORP11 knockout cells demonstrate reduced sphingomyelin levels. (A) CERT, ORP9 and ORP11 knockouts demonstrate decreased sphingomyelin and increased glucosylceramide levels. (B) Schematic representation of *de novo* sphingomyelin synthesis pathway of mammalian cells. (C) Decreased sphingomyelin and increased glucosylceramide levels observed in knockout cells are present in various sphingolipid subspecies. (D) Similar to CERT knockouts, ORP9 and ORP11 knockouts are sensitive to methyl-β-cyclodextrin treatment. (E) Western blot of knockout cells showing that loss of ORP9 or ORP11 does not affect CERT protein levels. (F) ORP9 and ORP11 localize at the Golgi apparatus. Scale bar 10μm. (G) Domain architecture of CERT, ORP9 and ORP11. All proteins contain PH domains for Golgi localization. ORP11 does not contain a FFAT motif.

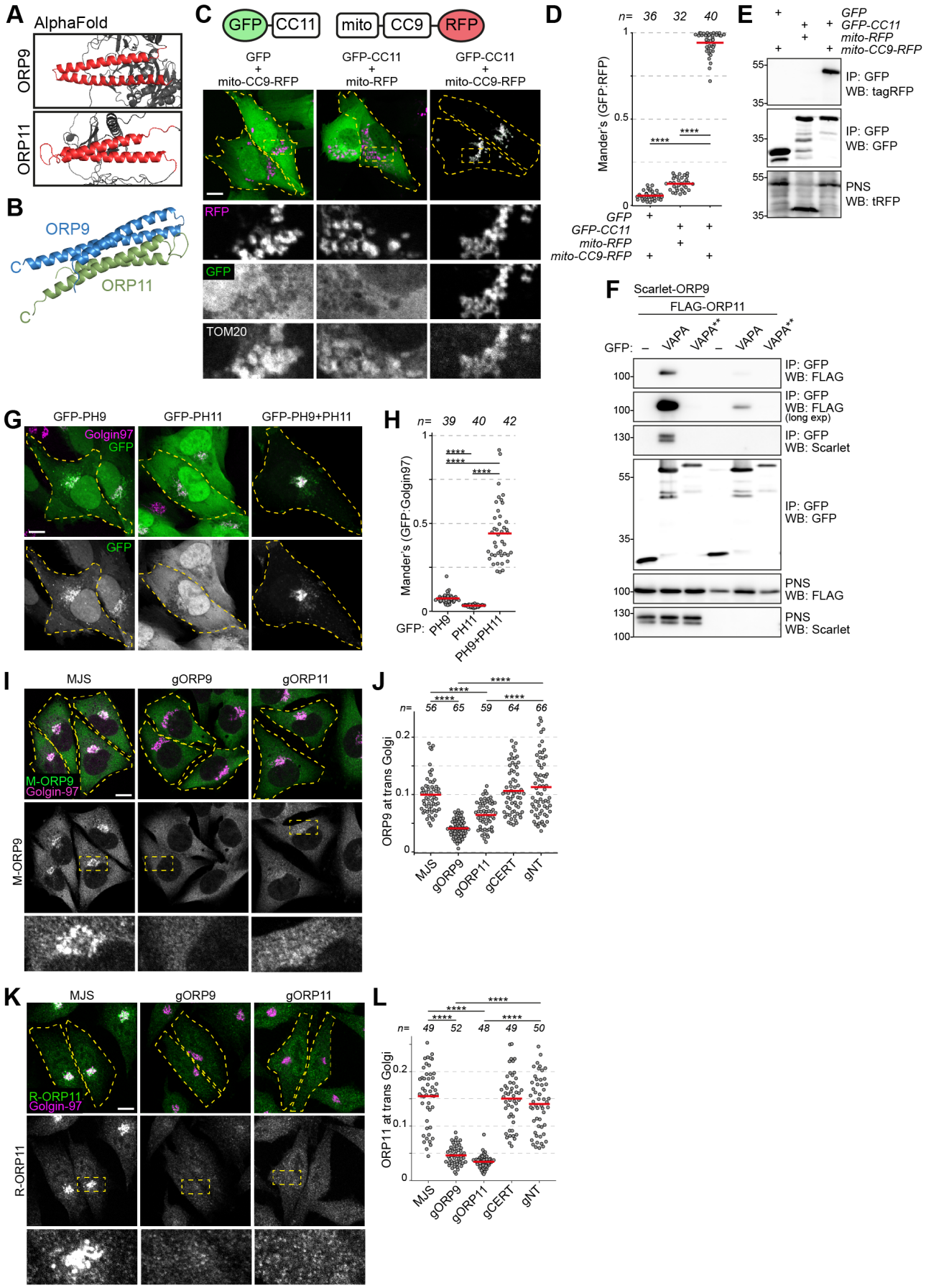

Figure 3: ORP9 and ORP11 dimerization is critical for their localization to ER-Golgi contact sites. (A) AlphaFold reveals two alpha-helices (coiled coils) in ORP9 and ORP11. (B) AlphaFold-Multimer shows that coiled coils of ORP9 and ORP11 interact with each other. (C) Coiled coils of ORP9 and ORP11 is sufficient

to define their localization as ORP11 coiled coils colocalizes with the mitochondria-targeted ORP9 coiled coils on mitochondria. (D) Colocalization analysis of immunofluorescent images from panel C. (E) Co-immunoprecipitation analysis confirming that coils of ORP9 and ORP11 interact with each other. (F) Co-immunoprecipitation analysis showing that despite lacking a FFAT motif, ORP11 interacts with the ER-resident VAPA protein. This interaction is facilitated by the FFAT motif of ORP9 as a VAPA mutant unable to interact with FFAT motifs (VAPA**) was unable to interact with ORP9 or ORP11. (G) Compared to individual PH domains of ORP9 and ORP11, ORP9-ORP11 chimera demonstrates better affinity towards the Golgi. (H) Colocalization analysis of immunofluorescent images from panel G. (I) ORP9 fails to localize at the Golgi as efficiently in ORP11 knockout cells. See Figure S7 for full panel. (J) Colocalization analysis of immunofluorescent images from panel I. (K) Similar to ORP9, ORP11 fails to localize at the Golgi as efficiently in ORP9 knockout cells. See Supplementary Figure S7 for full panel. Scale bar 10μm. (L) Colocalization analysis of immunofluorescent images from panel K.

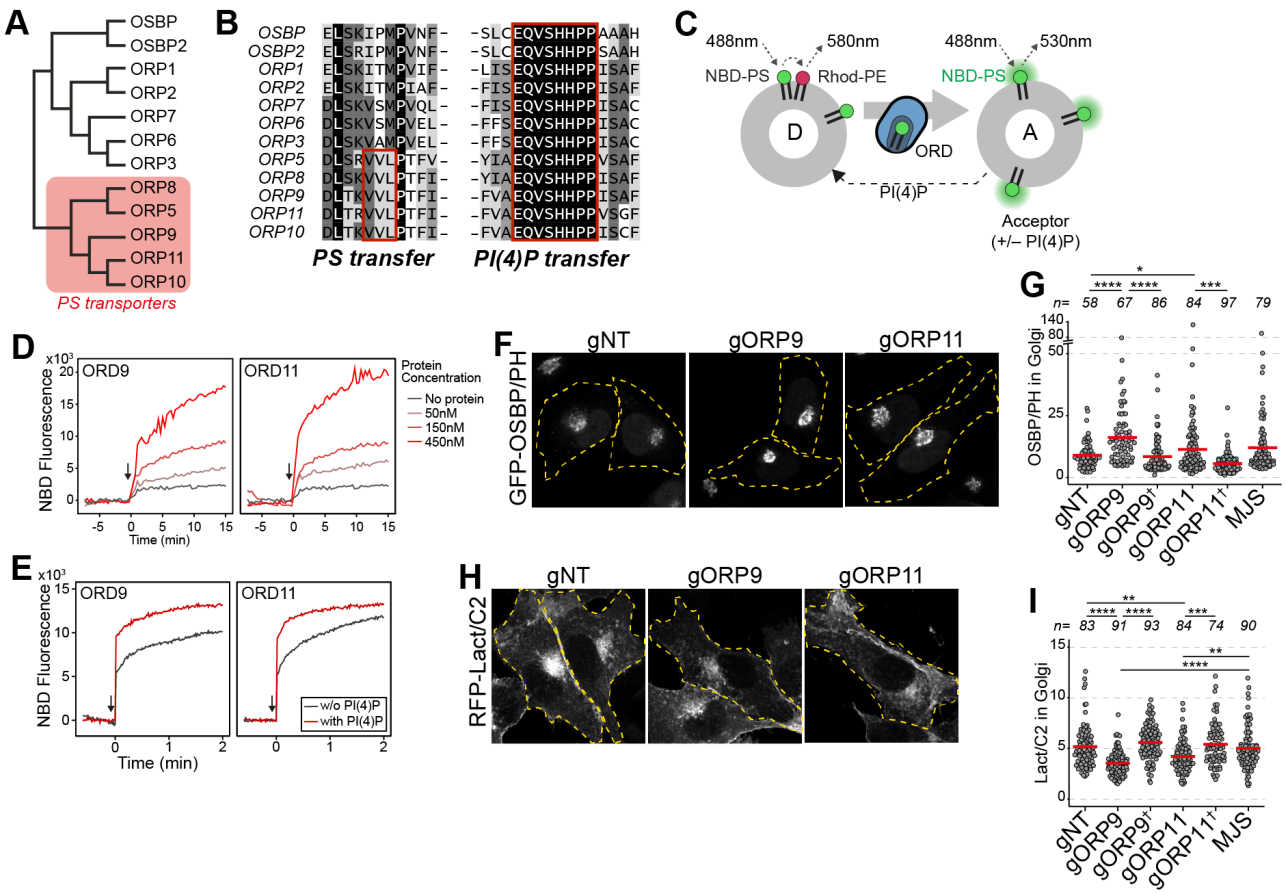

Figure 4: ORP9 and ORP11 are essential for PS / PI(4)P levels in the Golgi apparatus.
(A) Phylogenetic tree of human OSBP-related domains showing that ORP9 and ORP11 belong to the PS transporter branch. (B) ORP9 and ORP11 contain the critical residues for PS transfer. (C) Schematic representation of FRET-based lipid transfer assay. Rhodamine in the donor vesicles quenches NBD fluorescence unless NBD-labeled lipid is transferred to acceptor liposomes. (D) Lipid transfer assay using the OSBP-related domains of ORP9 and ORP11, ORD9 and ORD11 respectively, demonstrate the PS trafficking ability between vesicles *in vitro*. (E) PS transfer activity of ORD9 and ORD11 is promoted by addition of PI(4)P to acceptor liposomes, suggesting counter transfer of PI(4)P. (F) PI(4)P sensor localizes more prominently to the Golgi area in ORP9 and ORP11 knockout cells. See Figure S8 for full panel. (G) Golgi quantification of the PI(4)P sensor OSBP-PH localization reveals accumulation of PI(4)P at this organelle. This phenotype was rescued by reconstitution of the missing protein in knockout cells (shown with dagger). (H) PS sensor localizes less prominently to the Golgi in ORP9 and ORP11 knockout cells. See Figure S8 for full panel. (I) Golgi quantification of the PS sensor RFP-LactC2 indicates reduced PS levels in this organelle. This phenotype could be rescued by reconstitution of the missing protein in knockout cells (shown with a dagger).

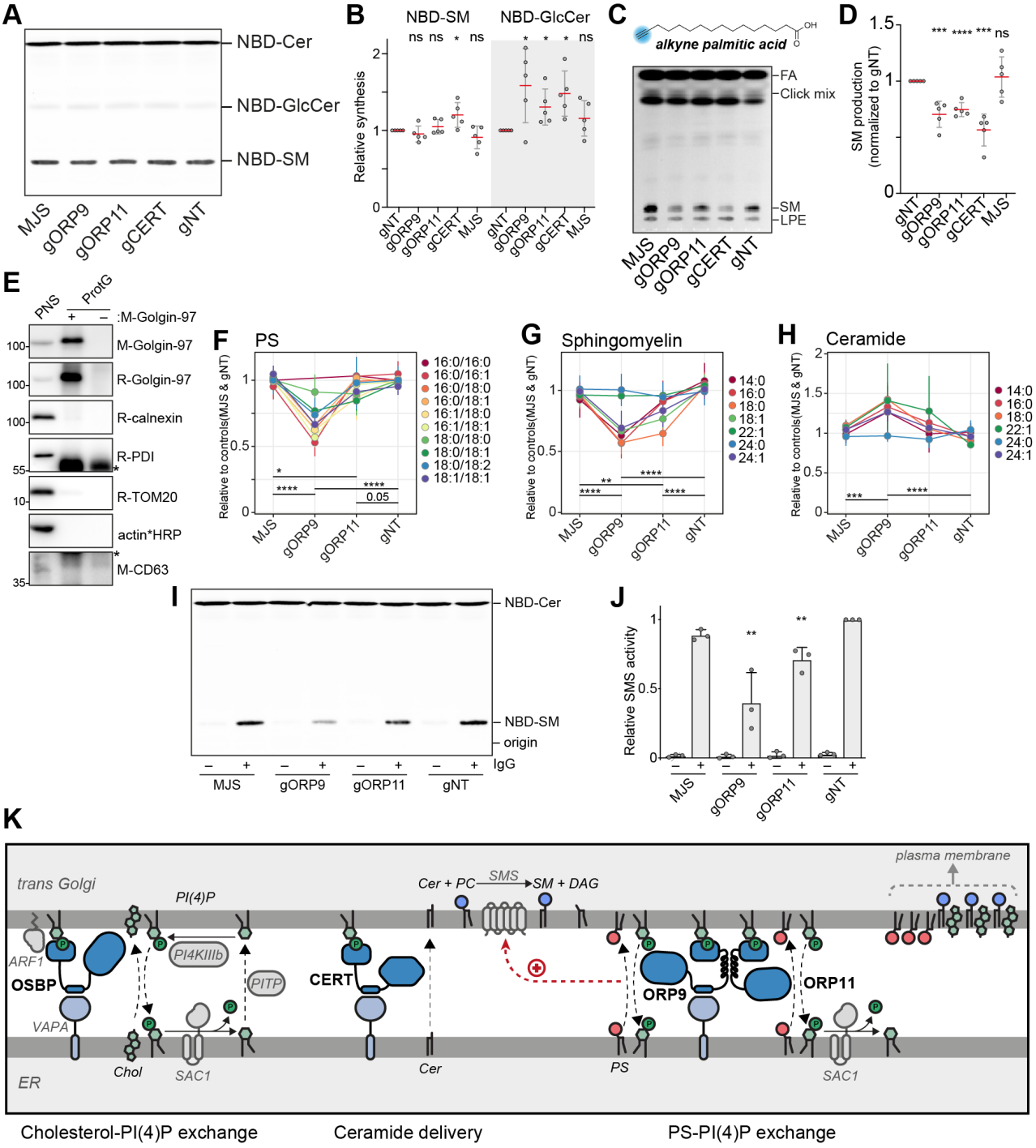

Figure 5: ORP9 and ORP11 are needed for *de novo* synthesis of sphingomyelin in the Golgi apparatus. (A) Thin-layer chromatography readout of the enzymatic activity assay performed in microsomes reveals the unreduced sphingomyelin synthesis capacity of knockout cells. (B) Quantification of the enzymatic activity assays from panel A. (C) Thin-layer chromatography readout of *de novo* sphingomyelin synthesis assay in intact cells using palmitic acid alkyne demonstrates the reduced conversion of palmitic acid alkyne to sphingomyelin. (D) Quantification of de novo sphingomyelin synthesis assay from panel C. (E) Western blot confirming the immunomagnetic isolation of *trans* Golgi membranes. (F-H) Lipidomics analysis of Golgi show lowered PS levels in the Golgi of ORP9 and ORP11 knockout cells. Same Golgi have reduced sphingomyelin but increased ceramide levels. Each line corresponds to a lipid species. n=4 experiments. (I) Thin-layer chromatography readout of enzymatic activity assay performed in isolated Golgi from knockout cells. Golgi of ORP11 and especially that of ORP9 demonstrate lowered capacity to synthesize sphingomyelin. (J) Quantification of sphingomyelin synthesis activity assay performed in Golgi isolates from panel I. (K) Model of ORP9-ORP11 mediated promotion of sphingomyelin synthesis. ORP9 and ORP11 require dimerization to localize at ER-trans Golgi membrane contact sites, where they exchange PS for PI(4)P. The same contact site

also accommodates OSBP and CERT for the anterograde trafficking of cholesterol and ceramide, the latter is used for sphingomyelin production. Cholesterol, sphingomyelin and PS are trafficked to the plasma membrane by vesicular means to be asymmetrically distributed between the leaflets of the plasma membrane.